



---

# Automatic detection of the cornea location in video captures of fluorescence

Tobin A. Driscoll<sup>1</sup>, Richard J. Braun<sup>1</sup>, Carolyn G. Begley<sup>2</sup>

<sup>1</sup>*Department of Mathematical Sciences, University of Delaware, Newark, DE, USA,*

<sup>2</sup>*School of Optometry, Indiana University, Bloomington, IN, USA*

## Abstract

**Purpose:** Fluorescence imaging is a valuable tool for studying tear film dynamics and corneal staining. Automating the quantification of fluorescence images is a challenging necessary step for making connections to mathematical models. A significant part of the challenge is identifying the region of interest, specifically the cornea, for collected data with widely varying characteristics.

**Methods:** The gradient of pixel intensity at the cornea–sclera limbus is used as the objective of standard optimization to find a circle that best represents the cornea. Results of the optimization in one image are used as initial conditions in the next image of a sequence. Additional initial conditions are chosen heuristically. The algorithm is coded in open-source software.

**Results:** The algorithm was first applied to 514 videos of 26 normal subjects, for a total of over 87000 images. Only in 12 of the videos does the standard deviation in the detected corneal radius exceed 1% of the image height, and only 3 exceeded 2%. The algorithm was applied to a sample of images from a second study with 142 dry subjects. Significant staining was present in a substantial number of these images. Visual inspection and statistical analysis show good results for both normal and dry-eye images.

**Conclusion:** The new algorithm is highly effective over a wide range of tear film and corneal staining images collected at different times and locations.

**Keywords:** Automated detection, Dry eye syndrome, Fluorescence, Tear film breakup

---

**Correspondence:** Department of Mathematical Sciences, University of Delaware, Newark, DE, USA.

E-mail: driscoll@udel.edu

---

## 1. Introduction

Dry eye is a condition affecting the ocular surface, characterized by a loss of homeostasis of the tear film. An unstable tear film leads to regions of tear thinning and inadequate lubrication the ocular surface, which can result in inflammation and ocular surface damage.<sup>1</sup> Clinical assessment of the unstable tear film involves timing the appearance of dark spots, termed tear breakup, following instillation of sodium fluorescein dye into the eye.<sup>2,3</sup> Fluorescein dye is also used to assess the extent of corneal damage or stained cells using grading scales.<sup>4–7</sup>

Both the assessment of corneal staining and tear film instability tests begin with the instillation of fluorescein dye, and both involve subjective clinical judgments. The tear film stability test times the appearance of a dark spot of tear breakup in the fluorescent tear film, but the judgment of “darkness” is undefined and may vary widely among clinicians.<sup>8</sup> In addition, timing is the only measure; the formation and rate of development of subsequent tear breakup is not included in the measurement.<sup>9</sup> Similarly, the severity of corneal damage, which is judged by fluorescein staining, is typically graded based on the extent of the corneal staining, using rather coarse scales ranging from Grade 0 (no staining) to Grades 3, 4 or 5 (severe staining, depending on the scale).<sup>4–7</sup> The subjective nature of these clinical tests has led to several attempts to automate the processes to improve the accuracy of both the fluorescein tear breakup time and corneal staining tests.<sup>10–16</sup> For this reason, we seek a method to automatically detect and dynamically measure areas of TBU and corneal staining from photographs or videos captured by the slit lamp biomicroscope, thus requiring only standard clinical equipment to capture tear film images.

A major step toward automatic detection of TBU or corneal staining is a reliable means of locating the cornea in each image, allowing us to exclude irrelevant regions. Some of the challenges that need to be overcome for successful cornea detection include off-center position within the image frame, motion and blurring during video capture, occlusion by eyelids and eyelashes that changes during partial and full blinks, variation in total illumination from one trial to another, visible physiological detail within a light-colored iris, changes in pupil size, and edges and structures interior to the image over the cornea.

Prior work in this vein (as described in a recent survey<sup>17</sup>) includes Ramos et al.<sup>18,19</sup>, who used Canny edge detection followed by maximizing correlation of the relevant edges with a predetermined set of circular and elliptical templates. Some of the details (e.g., Canny parameters, number of templates) were not specified. Furthermore the work was based on just 18 videos, and the published images show relatively favorable circumstances for cornea detection. Remeseiro et al.<sup>20</sup> faced a similar task for 44 lipid interferometry images. Their method first identified the pupil through cross-correlation of a thresholded image with circular templates, then found a concentrically located region of interest based on an empirical lower threshold for pixel luminosities. Chun et al.<sup>14</sup> applied automated processing to detect staining; for cornea detection they refer to a method of Daugman<sup>21</sup> that has similarities to ours. Su et al.<sup>22</sup>

trained a deep convolutional neural network to identify small square patches within an image as belonging to eyelids, eyelashes, sclera, or cornea, in the last case further distinguishing between TBU and non-TBU patches.

In this work we describe a new computational procedure for predicting the cornea location. It relies on gradients in image intensity at the cornea-sclera limbus without imposing further edge detection heuristics, and it uses continuous optimization rather than statistical correlations with a predetermined set of boundary templates. It has been applied to a data set consisting of more than 87,000 images within 514 videos, taken of 26 normal subjects, and to dry eye corneal staining images from a study with 142 subjects, some with severe staining. In both cases, the method showed good performance under all of the challenging conditions described above. Furthermore, our implementation of the method is available as open-source code.<sup>23</sup>

## 2. Methods

We use two data sets in this study. The first, as described in Awisi-Gyau et al.<sup>24</sup>, was from a study of tear breakup and the ocular surface sensory response to tear breakup that included twenty-six normal subjects. The second study included 142 DED subjects and was designed to develop a novel method for grading corneal staining.<sup>25</sup> Both studies received approval from the Biomedical Institutional Review Board of Indiana University. Declaration of Helsinki principles were followed during data collection and informed consent was obtained from subjects.

In the first study, subjects were seated behind a slit lamp biomicroscope. Two microliters of 2% fluorescein dye was instilled into the eye with a micropipette and subjects were asked to keep the tested eye open as long as possible. Images of the tear film were recorded at 16x magnification with a cobalt blue filter over the illumination system and a Wratten #12 filter over the observation port of the slit lamp biomicroscope. This lighting system causes the aqueous layer of the tear film (TF) and any corneal staining to fluoresce green. Videos were captured variously at 4 or 5 frames per second, depending on the subject, with the goal of filming a single interblink period.

We refer to a trial in this dataset as a sequence of consecutively captured images of the subject's eye. These images have resolution  $2824 \times 4240$ . In order to speed up subsequent input and processing, each image was first reduced by 50% in each dimension using ImageMagick version 7.0.10-22 with standard `-resize` option, resulting in resolution  $1412 \times 2120$ .

In the second study on corneal staining, 5 microliters of fluorescein dye was instilled into the tested eye and single photographs of corneal staining were taken using the same equipment setup as in the first study. Photographs were taken every 30 seconds for a period of five minutes or until the fluorescein dye was visibly washed out. The same procedure was repeated for the left eye.

Each video frame or photograph is an image with red, green, and blue channel

intensities, which we represent as the arrays  $R$ ,  $G$ , and  $B$ . Each is  $m \times n$ , with  $m$  and  $n$  being the number of rows and columns, respectively. The individual intensity values in each channel are normalized to be real numbers between zero (no intensity) and one (full intensity).

For detection we model the cornea as a circle, leaving us to determine its center ( $i_c, j_c$ ) and radius  $r_c$  in each video frame. We allow these to be real values rather than restricting them to integers. A circle is a more restricted model than, say, an ellipse. Estimates of mean vertical and horizontal diameters of the cornea include 10.6 mm and 11.7 mm, respectively<sup>26</sup> and 10.63 mm and 11.46 mm, respectively<sup>27</sup>, suggesting a difference of 10% or less between these measurements. We judge this to be of little concern for our purposes, and the use of a circle may be more robust in the presence of bright staining near the limbus that an ellipse may exclude more readily.

The feature we seek to exploit is the sharp increase in fluorescent intensity at the cornea-sclera limbus, as measured by a gradient in the outward radial direction. Maximization of the total gradient is the criterion used to select the center and radius of the model circle.

## 2.1 Purkinje image detection

The Purkinje image (i.e., the catoptric image of the illuminating source) serves as a landmark for initializing the optimization procedure described in section 2.3. It also is a small region of sharp intensity gradient that can interfere with the optimization, so it is preferable to detect and screen it out first.

In the data from normal subjects, the Purkinje image is distinguished in virtually all of the images by having a relatively strong pixel intensity in each of the red, green, and blue color channels. For these images we use the blue channel to detect the Purkinje image. In the dry-eye data, which features little data in the red and blue channels, we use the green channel. For what follows we use  $X$  to denote the array of intensity values in the selected channel.

In many, but not all, of our data images, the Purkinje image is at or near the maximum intensity of 1. We therefore use an adjustable threshold value  $\tau$  that determines the minimum intensity for the core of the Purkinje image. Starting with  $\tau = 0.95$ , the algorithm finds the rectangle of maximum area where  $X$  exceeds  $\tau$ . If the area is too small, then  $\tau$  is lowered by 0.05, because there aren't any clusters of sufficiently bright pixels, and the largest rectangle is found at the new threshold. Otherwise, the candidate rectangle must pass two tests. First, its height must exceed 80% of its width, in order to eliminate horizontally oriented bright lines at the eyelids. Second, the average pixel value inside the rectangle must exceed the value in a larger region surrounding it, in order to filter out the sclera. If these criteria are not met, the rectangular region is excluded from consideration and a new largest rectangle is found.

Finding a rectangle inscribed inside the Purkinje image is sufficient for estimating the cornea location as described in section 6. It can also be used to seed a growth algorithm to select adjacent similar pixels. Prior to detection, we enlarge the resulting

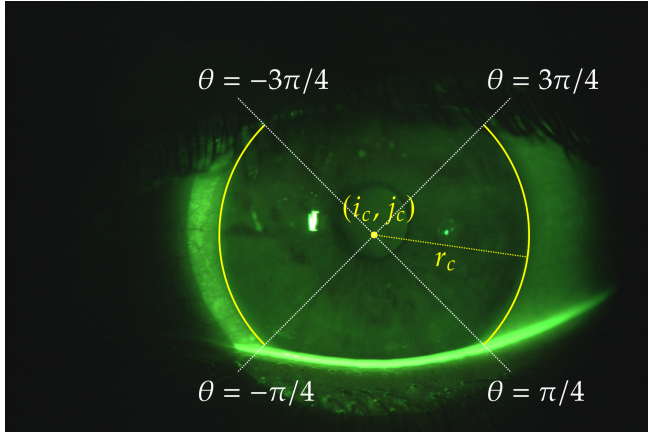


Fig. 1. Diagram showing a circle superimposed on a fluorescence image. The circle is determined by its center and radius. In order to reduce interference from eyelids and eyelashes, only the arcs shown are used to calculate the intensity gradient that will be maximized, as indicated by equation (1).

region and set the green intensity value to the median of an enclosing box, in order to mask the intensity gradient from the optimization process.

## 2.2 Intensity gradient

For any proposed cornea center  $(i_c, j_c)$  and radius  $r_c$ , we compute the outward radial gradient of intensity by finite differences at selected angles  $\theta_k$  lying one degree apart. Because the eyelids may obscure parts of the cornea's edge and also have bright lines that confuse the gradient, we select only  $\theta_k$  such that

$$\frac{\pi}{4} \leq |\theta_k| \leq \frac{3\pi}{4}, \quad (1)$$

as measured counterclockwise from the downward direction (the direction of increasing row index). See Fig. 1 for a diagram of the relevant angles.

Since the fluorescence is almost entirely green, we use only the  $G$  channel. To mitigate noise, we first apply to  $G$  a Gaussian filter of standard deviation  $m/80$  in all directions. The blurred pixel values can then be interpolated linearly to off-grid values, defining the intensity function  $z(i, j)$ . We shift to polar coordinates relative to the proposed cornea center via

$$\tilde{z}(r, \theta) = z(i_c + r \cos(\theta), j_c + r \sin(\theta)). \quad (2)$$

Finally, the radial gradient at angle  $\theta_k$  is approximated by

$$g(\theta_k) = \tilde{z}(r_c + 2, \theta_k) - \tilde{z}(r_c - 2, \theta_k). \quad (3)$$

### 2.3 Optimization and serial processing

With the preprocessing and definitions described above, the objective of the optimization step is to maximize over  $i_c, j_c, r_c$  the value of

$$\sum_k g(\theta_k), \quad (4)$$

with the gradient values  $g(\theta_k)$  defined in (3) and the sum taken over all included angles  $\theta_k$ . We also added logarithmic barrier functions with to enforce the restrictions  $1 \leq i_c \leq m, 1 \leq j_c \leq m$ , and  $0.25m \leq r_c \leq 0.6m$  in unconstrained methods, though one could alternatively use box constraints in a constrained optimization method.

The optimization step runs very quickly compared to other operations in the processing chain, so we apply both a trust-region quasi-Newton method and the Nelder–Mead method to each of several initial conditions, retaining the best result from among all cases. The initial conditions selected are the optimal state found in the preceding video frame (if any); the generic values  $i_c = m/2, j_c = n/2, r_c = m/2.7$ ; and the heuristic values obtained by the algorithm described in the Appendix.

## 3. Results

The algorithms described in section 2 were implemented in Julia 1.5 as open-source software<sup>23</sup> and run in Ubuntu 18.04.5. Apart from file loading times, each image took around a second to process.

### 3.1 Analysis of tear breakup images

Fig. 2 shows the results of the cornea detection on individual images taken from videos of nine different subjects. As shown in Table 1, these images exemplify a variety of challenging conditions for detection. Partial occlusion by the eyelids occurs in most of the collected images, and eyelashes often significantly cover the superior cornea, as in examples (b)and (d)–(g). Corneal staining appears as light colored dots or areas, as seen in images (b), (c), and (i). Structures in a light-colored iris create a pattern of light and dark features beneath the cornea (examples (c) and (i)) that are not seen in images of dark-colored irises. These features can create false negatives for standard edge detection methods. Reflex tearing, as in image (a), can also create spurious edges in the image. Many images are captured before the slit lamp is turned on (example (h)) or do not show much of the limbus simultaneously on both left and right sides of the cornea (examples (e) and (g)). Finally, the detection method does not rely on preprocessing, registration, or stabilization in order to a priori constrain the cornea near the center of the image, as demonstrated in examples (a) and (d)–(g).

Fig. 3 shows time traces of the detected cornea center and radius for 12 trials taken from four subjects. The cornea center ( $i_c, j_c$ ) and radius  $r_c$  are normalized by the

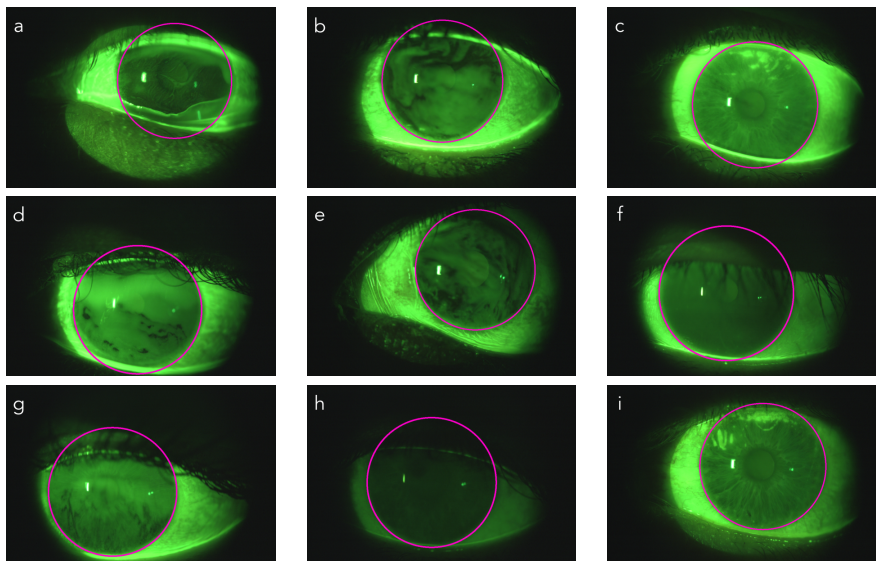


*Fig. 2.* Results of cornea detection on video frames from nine different subjects. The detected cornea region is shown in each case by a magenta circle. See text and Table 1 for a description of features in individual images.

*Table 1.* Challenging features of the images in Fig. 2.

	(a)	(b)	(c)	(d)	(e)	(f)	(g)	(h)	(i)
Occlusion by eyelid	✓	✓	✓	✓		✓	✓	✓	
Corneal staining		✓	✓						✓
Eyelashes	✓			✓		✓	✓	✓	
Light-colored iris				✓					✓
Reflex tearing					✓				
Poor illumination						✓	✓		
Off-center location	✓			✓	✓	✓	✓	✓	

height of the image ( $m = 1412$  pixels), and the traces show the differences between these normalized values over time and their median values over the entire trial. Many videos in the set begin before the slit lamp biomicroscope is turned on and/or end with one or more blinks. These periods cause the large jumps in the time traces seen near either end of some of the time series in Fig. 3, and they are not of interest.

Fig. 4 shows an assessment over the entire data set of the consistency of the cornea detection algorithm via the variability in the detected radius  $r_c$ . Out of 514 videos, only 12 cases (2.3%) show a standard deviation greater than 1% of the image height, and just 3 are above 2%. These small values, combined with visual spot checks of the results, give us high confidence in nearly all of the detection results. Typically, the failure mode in the worst cases involves a side of the limbus moving out of the illuminated area or being obscured due to high exposure that reduces contrast.

In Fig. 5 and Fig. 6 we show the processed images comprising the shaded regions A and B of Fig. 3. In the interblink period, the paths of  $i_c$  and  $j_c$  should indicate unsteadiness, drift, and occasional rapid movement in the position of the eye within the image frame. In Fig. 5, for example, we can see considerable motion blur corresponding to rapid movement of the cornea relative to the frame rate of the camera. This movement is reflected in a sudden increase of the red curve and decrease of the blue curve in region A of Fig. 3.

Changes in the detected radius  $r_c$  may result from physical changes in the cornea-camera distance, but we expect and observe these motions to be smaller than the transverse ones. These changes may also be nonphysical artifacts of the detection process, as illustrated in Fig. 6. During frames (d-f) of this time series, the upper eyelid occludes a slightly larger portion of the cornea than just before. Combined with the lack of visible limbus on the left side of the cornea due to poor illumination, this causes a small temporary increase in the detected cornea radius, though the detected portion over the cornea looks passable throughout the series.

### 3.2 Analysis of corneal staining images

In Fig. 7 we see that the results of applying the algorithm to detection of the cornea in images taken from subjects with DED. Some of these images bring challenges beyond the images of normal subjects. DED subjects may have greater difficulty keeping their eyelids wide open for an extended period of time, leading to greater occlusion of the cornea. Some show extensive staining with significant coalescence and intensity. Examples (a), (b), (e), and (h) show areas of coalesced staining, which can hinder corneal detection because the stained areas are difficult to distinguish from the conjunctiva. Fainter, lesser amounts of corneal staining appear to have less effect. In addition, most of the issues in Table 1 also affect images of corneal staining. Nonetheless, the algorithm performs excellently on all of them.

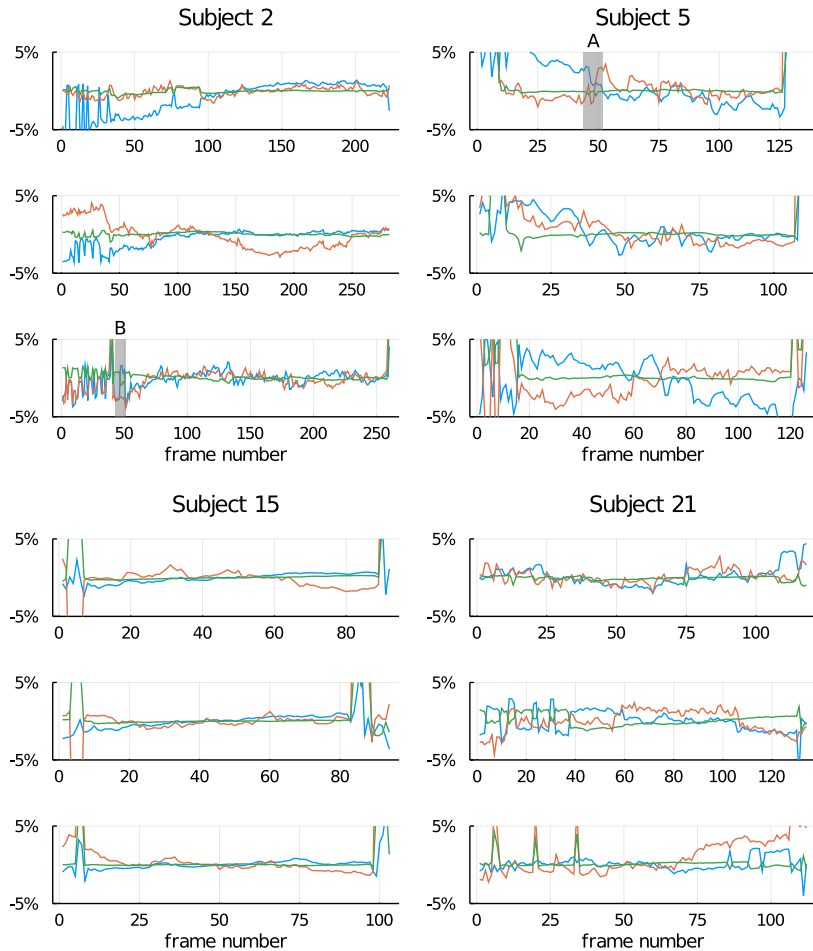


*Fig. 3.* Detected center and radius of the cornea over time. For each trial, the cornea center ( $i_c, j_c$ ) and radius  $r_c$  are normalized by the height of the image ( $m = 1412$  pixels), and the difference between the each value and its median over the trial is plotted (blue, red, and green for  $i_c, j_c$ , and  $r_c$ , respectively). The labels A and B refer to image sets in subsequent figures.

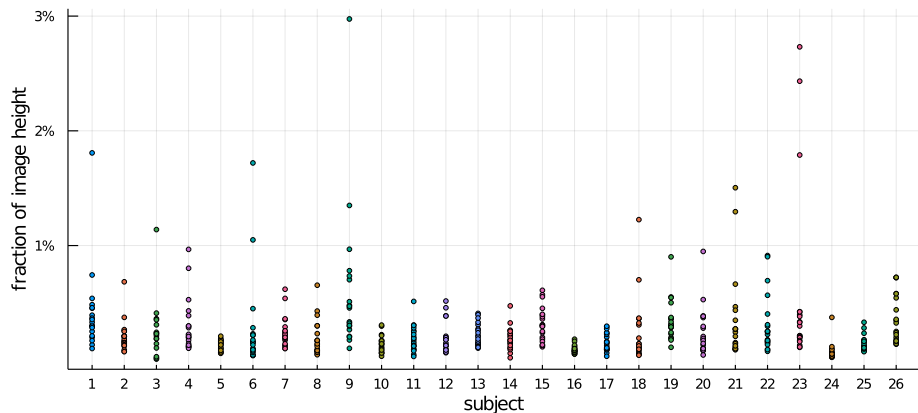


Fig. 4. Standard deviation of  $r_c$  over the course of each video during the interblink period of interest. Results are grouped by subject; most subjects have 20 values reported.

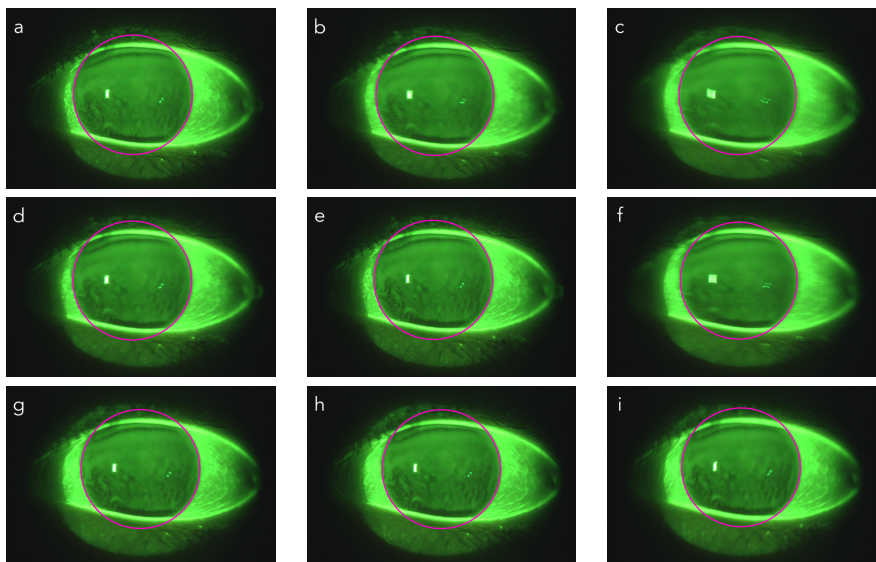


Fig. 5. Set of images from a trial for subject 5. The period marked as shaded region A in Fig. 3 consists of the nine consecutive processed images shown here. The detected cornea for each image is shown by a magenta circle. The cornea is tracked accurately while moving upward and to the right; note the motion blur in (b), (c), and (f).

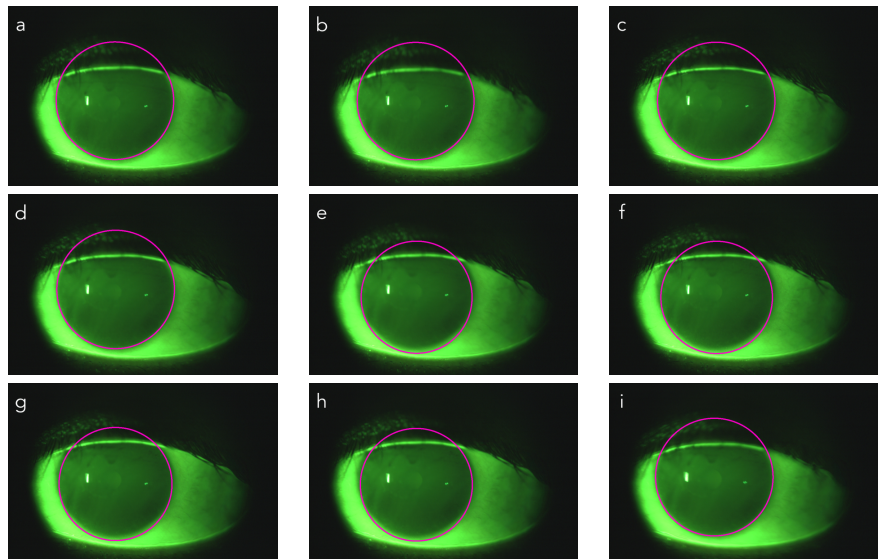
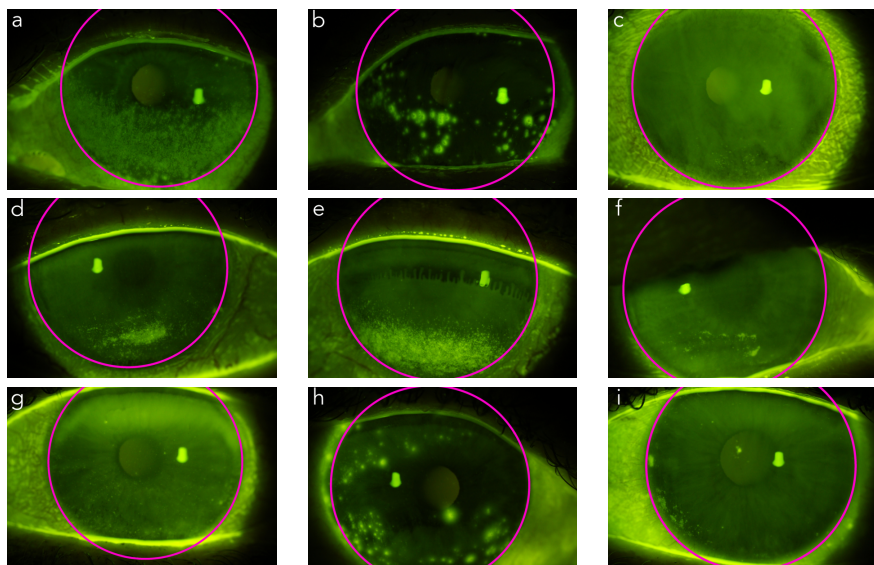


Fig. 6. Set of images from a trial for subject 2. The period marked as shaded region B in Fig. 3 consists of the consecutive processed images shown here. The detected cornea is shown by a magenta circle. Subtle changes in the upper eyelid occlusion caused a temporary nonphysical change to the detected radius in (e)–(h).



*Fig. 7. Sample cornea detection in images of the tear film in 9 different eyes with DED. Cases (a), (b), (e), and (h) exhibit extensive staining, and cases (a), (b), (d), (e), and (f) have high levels of eyelid occlusion.*

## 4. Discussion

The methods described in this study successfully detected the cornea from both videos of fluorescein tear breakup and corneal staining in DED subjects. Thus, this method can be used for the first step of automating either clinical test, which provides needed objectivity to these highly subjective tests.

We believe that these are the first published results demonstrating a high degree of effectiveness at cornea detection over a wide range of patients, including DED patients, and a large data set. The robust and consistent performance in the presence of challenging factors such as eyelid occlusion, extensive corneal staining, eyelashes, light-colored iris, reflex tearing, inconsistent illumination, and rapid movement is critical to future applications in clinical settings, particularly for patients with DED.

A critical component of the success of the software is to search for the limbus over only part of a proposal circle, rather than the entire circle. This minimizes interference from the upper and lower eyelids. Our inspections of the results confirm that the restriction to circular models over more general shapes is justified.

## 5. Conclusions and future perspectives

We have created free and open-source software implementing new algorithms for detecting the cornea within video captures of fluorescent tear films and images of

corneal staining. The method is robust over a wide range of challenging circumstances observed in the course of 514 videos of 26 normal subjects, comprising about five total hours of video footage. Corneal staining images add challenges on top of those for the tear films. Our method was demonstrated to be highly successful through visual inspections and statistical analysis.

Future work could use reliable detection of the cornea as a first step in, for instance, automated image segmentation or machine learning assessments of tear film breakup, or for automated graded of staining severity. Another direction would be to try ellipses instead of circles as the cornea model, increasing the number of free parameters from 3 to 5 (adding orientation and eccentricity, for example). The availability of the code allows further applications to data sets generated by clinicians for normal and dry-eye patients.

## Acknowledgments

This work was supported by National Science Foundation grant DMS 1909846. The content is solely the responsibility of the authors and does not necessarily represent the official views of the funding sources.

## 6. Appendix: Heuristic initial condition for optimization

In addition to using generic values and the results of the preceding frame to initialize the cornea parameters  $i_c$ ,  $j_c$ , and  $r_c$ , a heuristic method is applied to find two other initializations that are attempted by the optimization method. This process begins by finding the location of a rectangle inscribed in the Purkinje image as described in section 2.1. The vertical midpoint of this rectangle is used for  $i_c$  in both of the initializations described here.

Two choices are found for the other cornea circle parameters. In most frames there is a substantial amount of bright sclera to the left and right of the cornea. We want to use the edges of the sclera to initialize  $j_c$ . We begin by selecting all pixels  $(i, j)$  such that  $G_{ij} > 0.5 \max_{i,j} G_{ij}$ , excluding those previously identified as belonging to the Purkinje image. Our method will be to locate the left and right peaks of the distribution of the column indices of these pixels. We represent this distribution by binning them into 100 bins between 1 and  $n$ . Let  $j_L$  be the center of the bin with the most hits for indices less than  $n/2$  (i.e., in the left half of the image), and similarly let  $j_R$  be the center of the bin with the most hits for indices greater than  $n/2$ . Then our first estimates of  $j_c$  and  $r_c$  are

$$j_c = \frac{j_R + j_L}{2}, \quad r_c = \frac{j_R - j_L}{2}. \quad (5)$$

Some images do not include much if any of the sclera to one side of the cornea, making  $j_L$  or  $j_R$  unreliable or infeasible to obtain. Our other initialization is meant to

help with these situations. We describe it here when  $j_R$  is known, but the other case is similar. We give a parameter  $-1 < \gamma < 1$  that describes the approximate expected position of the Purkinje image relative to the corneal center and normalized by the corneal radius. Let  $j_M$  be the median value of the column indices for the Purkinje image. Then the geometry implies

$$\tilde{r}_c = \frac{j_R - j_M}{1 - \gamma}, \quad \tilde{j}_c = j_R - \tilde{r}_c \quad (6)$$

for the second initialization.

## References

1. Craig JP, Nichols KK, Akpek EK, Caffery B, Dua HS, Joo CK, et al. TFOS DEWS II Definition and Classification Report. en. The Ocular Surface. TFOS International Dry Eye WorkShop (DEWS II), July 2017;15(3): 276–283. ISSN: 1542-0124. doi: 10/gbstrp.
2. Norn MS. Desiccation of the Precorneal Film. en. Acta Ophthalmologica, 1969;47(4): 881–889. ISSN: 1755-3768. doi: 10/dj95jq.
3. Cho P, Brown B, Chan I, Conway R, Yap M. Reliability of the Tear Break-Up Time Technique of Assessing Tear Stability and the Locations of the Tear Break-Up in Hong Kong Chinese: en. Optometry and Vision Science, Nov. 1992;69(11): 879–885. ISSN: 1040-5488. doi: 10/fb4kjk.
4. Lemp MA. Report of the National Eye Institute/Industry Workshop on Clinical Trials in Dry Eyes. eng. The CLAO journal: official publication of the Contact Lens Association of Ophthalmologists, Inc, Oct. 1995;21(4): 221–232. ISSN: 0733-8902.
5. Bron AJ, Evans VE, Smith JA. Grading of Corneal and Conjunctival Staining in the Context of Other Dry Eye Tests. eng. Cornea, Oct. 2003;22(7): 640–650. ISSN: 0277-3740. doi: 10/d648xt.
6. Whitcher JP, Shibuski CH, Shibuski SC, Heidenreich AM, Kitagawa K, Zhang S, et al. A Simplified Quantitative Method for Assessing Keratoconjunctivitis Sicca from the Sjögren's Syndrome International Registry. eng. American Journal of Ophthalmology, Mar. 2010;149(3): 405–415. ISSN: 1879-1891. doi: 10/ckdjf2.
7. Terry RL, Schnider CM, Holden BA, Cornish R, Grant T, Sweeney D, et al. CCLRU Standards for Success of Daily and Extended Wear Contact Lenses. eng. Optometry and Vision Science: Official Publication of the American Academy of Optometry, Mar. 1993;70(3): 234–243. ISSN: 1040-5488. doi: 10/dw2dwf.
8. Norn MS. Tear Film Breakup Time: A Review. The Preocular Tear Film in Health, Disease and Contact Lens Wear. Lubbock, TX: Dye Eye Institute, 1986; 52–56.
9. Liu H, Begley CG, Chalmers R, Wilson G, Srinivas SP, Wilkinson JA. Temporal Progression and Spatial Repeatability of Tear Breakup. en-US. Optometry and Vision Science, Oct. 2006;83(10): 723–730. ISSN: 1538-9235. doi: 10/bsp8tf.
10. Amparo F, Wang H, Yin J, Marmalidou A, Dana R. Evaluating Corneal Fluorescein Staining Using a Novel Automated Method. eng. Investigative Ophthalmology & Visual Science, May 2017;58(6): BIO168-BIO173. ISSN: 1552-5783. doi: 10/gbmdx3.
11. Pritchard N, Young G, Coleman S, Hunt C. Subjective and Objective Measures of Corneal Staining Related to Multipurpose Care Systems. eng. Contact Lens & Anterior Eye: The Journal of the British Contact Lens Association, Mar. 2003;26(1): 3–9. ISSN: 1367-0484. doi: 10/bq32wm.
12. Wolffsohn JS, Purslow C. Clinical Monitoring of Ocular Physiology Using Digital Image Analysis. en. Contact Lens and Anterior Eye, Mar. 2003;26(1): 27–35. ISSN: 13670484. doi: 10/c26rht.
13. Tan B, Zhou Y, Svitova T, Lin MC. Objective Quantification of Fluorescence Intensity on the Corneal Surface Using a Modified Slit-Lamp Technique. eng. Eye & Contact Lens, May 2013;39(3): 239–246. ISSN: 1542-233X. doi: 10/f4xc3x.

14. Chun YS, Yoon WB, Kim KG, Park IK. Objective Assessment of Corneal Staining Using Digital Image Analysis. en. *Investigative Ophthalmology & Visual Science*, Dec. 2014;55(12): 7896–7903. ISSN: 1552-5783. doi: 10/f6txkr.
15. Pellegrini M, Bernabei F, Moscardelli F, Vagge A, Scotto R, Bovone C, et al. Assessment of Corneal Fluorescein Staining in Different Dry Eye Subtypes Using Digital Image Analysis. eng. *Translational Vision Science & Technology*, Nov. 2019;8(6): 34. ISSN: 2164-2591. doi: 10/ghwn39.
16. Sher I, Tzameret A, Szalapak AM, Carmeli T, Derazne E, Avni-Zauberan N, et al. Multimodal Assessment of Corneal Erosions Using Optical Coherence Tomography and Automated Grading of Fluorescein Staining in a Rabbit Dry Eye Model. eng. *Translational Vision Science & Technology*, Jan. 2019;8(1): 27. ISSN: 2164-2591. doi: 10/ghwn38.
17. Vyas AH, Mehta MA. A Comprehensive Survey on Image Modality Based Computerized Dry Eye Disease Detection Techniques. *Advances in Science, Technology and Engineering Systems Journal*, 2020;5(2): 748–756. ISSN: 24156698, 24156698. doi: 10/ghwn37.
18. Ramos L, Barreira N, Mosquera A, Penedo MG, Yebra-Pimentel E, García-Resúa C. Analysis of Parameters for the Automatic Computation of the Tear Film Break-up Time Test Based on CCLRU Standards. en. *Computer Methods and Programs in Biomedicine*, Mar. 2014;113(3): 715–724. ISSN: 0169-2607. doi: 10/f5tgrc.
19. Ramos L, Barreira N, Pena-Verdeal H, Giráldez MJ, Yebra-Pimentel E. Computational Approach for Tear Film Assessment Based on Break-up Dynamics. en. *Biosystems Engineering. Innovations in Medicine and Healthcare*, Oct. 2015;138, 90–103. ISSN: 1537-5110. doi: 10/f7stvd.
20. Remeseiro B, Mosquera A, Penedo MG, Garcia-Resúa C. Tear Film Maps Based on the Lipid Interference Patterns: Proceedings of the 6th International Conference on Agents and Artificial Intelligence. ESEO, Angers, Loire Valley, France: SCITEPRESS - Science and and Technology Publications, 2014; 732–739. ISBN: 978-989-758-015-4 978-989-758-016-1. doi: 10/ghwn4c.
21. Daugman J. How Iris Recognition Works. *IEEE Transactions on Circuits and Systems for Video Technology*, Jan. 2004;14(1): 21–30. ISSN: 1558-2205. doi: 10/bwxqsn.
22. Su TY, Liu ZY, Chen DY. Tear Film Break-Up Time Measurement Using Deep Convolutional Neural Networks for Screening Dry Eye Disease. *IEEE Sensors Journal*, Aug. 2018;18(16): 6857–6862. ISSN: 2379-9153. doi: 10.1109/jsen.2018.2850940.
23. Driscoll TA. Cornea Detection Software Package for Julia. Jan. 2021;
24. Awisi-Gyau D, Begley CG, Situ P, Simpson TL. Changes in Corneal Detection Thresholds After Repeated Tear Film Instability. en. *Investigative Ophthalmology & Visual Science*, Oct. 2019;60(13): 4234. ISSN: 1552-5783. doi: 10/ghwn4b.
25. Simpson T, Begley CG, Situ P, Feng, Nelson JD, Caffery B, et al. Canonical Grading Scales of Corneal and Conjunctival Staining Based on Psychophysical and Physical Attributes. *Translational Vision Science and Technology*, in review.
26. Duke-Elder S, Wybar KC. The Cornea. *The Anatomy of the Visual System. 2. System of Ophthalmology*. London: Henry Kimpton, 1961; 92–94.
27. Khng C, Osher RH. Evaluation of the Relationship between Corneal Diameter and Lens Diameter. en-US. *Journal of Cataract & Refractive Surgery*, Mar. 2008;34(3): 475–479. ISSN: 0886-3350. doi: 10 / dvknbj.